

Surface- and strain-tuning of the optical dielectric function in epitaxially grown CaMnO_3

Dominic Imbrenda¹, Dongyue Yang², Hongwei Wang², Andrew R. Akbashev¹,
Bruce A. Davidson², Xifan Wu², Xiaoxing Xi², and Jonathan E. Spanier^{1,3*}

¹*Department of Materials Science & Engineering,
Drexel University, Philadelphia, PA 19104, USA*

²*Department of Physics, Temple University, Philadelphia, PA 19104, USA and*

³*Department of Physics, Drexel University, Philadelphia, PA 19104, USA*

(Dated: September 22, 2022)

Abstract

We report an anomalously strong thickness dependence of the complex frequency-dependent optical dielectric function ($\tilde{\epsilon}(\omega)$) in epitaxial $\text{CaMnO}_3(001)$ thin films on $\text{SrTiO}_3(001)$, $\text{LaAlO}_3(001)$, and $\text{SrLaAlO}_4(001)$ substrates. A doubling of the peak value of the imaginary part of $\tilde{\epsilon}(\omega)$ and spectral shifts of 0.5 eV for a given magnitude of absorption are observed. On the basis of the experimental data and first-principles density functional theory calculations of $\tilde{\epsilon}(\omega)$, its evolution with thickness from 4 to 63 nm has several regimes. In the thinnest, strain-coherent films, the response is characterized by a significant contribution from the free surface that dominates strain effects. However, at intermediate and larger thicknesses approaching the bulk-like film, strain coherence and partial strain relaxation persist and influence $\tilde{\epsilon}(\omega)$.

*email: spanier@drexel.edu

Strain engineering has long been used as an effective way to tune electronic, magnetic and optical properties of oxide thin films [1, 2]. The lattice distortions imposed by epitaxial strain can introduce dramatic changes in the properties of thin-film materials, e.g. allowing strong ferroelectric ordering in quantum paraelectrics [3], manipulation of transition temperatures in ferroelectrics [4], tuning of magnetic and metal-insulator transitions in mixed-valence perovskite oxides [5, 6], and controlling the volume of the magnetic phase in magnetically inhomogeneous media [7]. Owing to the direct relationship between the electronic structure and optical properties, epitaxial strain strongly influences dielectric constants, refractive indices and, ultimately, the bandgap of a thin film material [8–10]. However, such studies for oxides are still scarce, and the roles of chemistry, structure, native defects (oxygen vacancies), film thickness of the film and surface effects (termination, admolecules, structural reconstruction) have yet to be clarified.

Here we study optical properties of CaMnO_3 (CMO) thin films that are epitaxially strained. In the bulk, electronic structure and optical properties of CMO are well studied [11–13], yet little attention has been given to the optical properties of epitaxial CMO thin films. CMO has long been known as an archetypal mixed-valence manganite that exhibits colossal magnetoresistance (CMR). However, strain-induced multiferroicity has also been predicted for CMO [2] with incipient ferroelectricity being later confirmed in tensile-strained films [14]. Similar to other perovskite oxides, CMO can easily accommodate oxygen vacancies that can be introduced allowing the material to demonstrate modest electrocatalytic activity [15, 16]. Still, little is known about the changes in the electronic structure in thin and ultrathin CMO films despite a certain surge of interest to strain-mediated effects on the optical properties of perovskite oxides [8–10, 17–19]. In addition, because surface reconstruction and termination become crucial in a few unit cell thick perovskite oxides, ultrathin CMO films are expected to demonstrate optical properties that are distinct from those of thicker films [20].

Here, we report pronounced thickness dependence of the complex frequency-dependent optical dielectric function ($\tilde{\epsilon}(\omega)$) in epitaxial CMO thin films. Using spectroscopic ellipsometry we perform detailed characterization of optical properties of CMO thin films, and we employ first-principle density functional theory (DFT) calculations to determine the contribution both from the surface states and epitaxial strain to the optical dielectric function of CMO.

Epitaxial CMO thin films were grown by pulsed laser deposition (PLD) using a KrF excimer laser ($\lambda = 248 \text{ nm}$) on (001)-oriented SrTiO_3 (STO), LaAlO_3 (LAO), and SrLaAlO_4

(SLAO) (Crystec). A laser repetition rate of 2.11 Hz and a laser energy density of 2.0 J/cm² were used. The substrate temperature was 650°C and the background pressure was around 8.6×10⁻⁶ Torr. The film was deposited in oxygen environment at 30 mTorr and after the deposition, the sample was cooled to room temperature within an oxygen environment around 300 Torr. The thickness of the film was measured by X-ray reflectivity (XRR) and the film deposition rate was characterized around 0.74 Å/pulse. Samples ranging from 4.1 - 63 nm in thickness were each grown on SrTiO₃ substrates(001), and samples ranging in thickness from 4.2 - 10 nm were grown on LAO and SLAO substrates. XRR (Fig. 1 (b)) and atomic force microscopy (AFM) (Fig. 1 (a)) were used to determine thickness and surface roughness; grazing incidence X-ray diffraction (GIXRD) (Fig. 1 (d)) and reciprocal space mapping (RSM) were used to determine film lattice strain.

Five CMO film samples of different thicknesses were grown on STO, and two additional films were grown, each on LAO and SLAO, to probe and disentangle the effects of thickness, strain and strain relaxation on $\tilde{\epsilon}(\omega)$ of CMO. The in-plane lattice parameter of STO ($a_{\text{STO}} = 3.905$ Å) is larger than that for LAO ($a_{\text{LAO}} = 3.79$ Å) or SLAO ($a_{\text{SLAO}} = 3.75$ Å), and largest compared to that for bulk CMO ($a_{\text{CMO}} = 3.72$ Å), resulting in persistence of in-plane CMO film tensile strain coherency in CMO/STO to smaller thicknesses than that for films on LAO or SLAO. The measured a_{CMO} for films grown on STO is the same for the two thinnest (approx. 11 and 16 unit cells) films, but relaxes to smaller values for the thicker films. A summary of the parameters for each film, including substrate, thickness, measured in-plane lattice parameter a , the corresponding in-plane strain, and surface roughness is shown in Table I.

Variable-angle spectroscopic ellipsometry (VASE) was performed at room temperature in ambient atmosphere with an electronically controlled rotating compensator and Glan-Taylor polarizers (J.A. Woollam, M2000). Measurements were performed at multiple angles between 65-75° and in the spectral range of 247-1000 nm with a resolution of 1.6 nm. To determine $\tilde{\epsilon}(\omega)$ for CMO we assume a four-layer optical medium comprised of a homogeneous isotropic film layer on a semi-infinite bulk, incorporating surface roughness, in vacuum. The surface roughness layer is modeled using the Bruggeman effective medium approximation using a 50% film and 50% void at the surface [21] with thickness equal to the root-means-squared roughness for each sample obtained from AFM. Our model accounting for surface effects is valid as long as the surface layers are thin compared to the bulk and have a refractive index

lower than that of the bulk [22]. Optical dielectric functions of each substrate from the same batch as those used for film growth were also determined, assuming a semi-infinite half-space in vacuum, and incorporated as the bulk layer in the model.

To fit the spectral dependence and calculate the complex index of refraction of each sample a combination of Gaussian curves and Lorentz oscillators were used to model the experimental data. The number and type of oscillators used was sample dependent. Both of these functions are Kramers-Kronig consistent which ensures causality. Regression analysis using the Levenberg-Marquardt algorithm was performed until the mean squared error (MSE) between the parameters and experimental data was minimized. Thickness of the film and surface roughness were determined from XRR and held constant in the model until a satisfactory fit was achieved. After obtaining an acceptable MSE the thickness and surface roughness were made free parameters to ensure good agreement of thickness between the model and XRR data. VASE- and XRR- determined thicknesses are given in Table I.

Fig. 2 displays that $\tilde{\epsilon}(\omega)$ depends sensitively on film thickness. For films grown on STO, increasing thickness is accompanied by progressive strain relaxation and evolution of $\tilde{\epsilon}(\omega)$. For our thickest, bulk-like film (62.9 nm) $\tilde{\epsilon}(\omega)$ is consistent with previously published data for bulk CMO crystals [12, 23]. For thinner films and increasing thickness fraction of strain coherence, to fully strain-coherent, there is reduction by as much as 50% of both the real and imaginary parts of $\tilde{\epsilon}(\omega)$. The linear portion of the optical absorption $\alpha(\omega) = 4\pi k/\lambda$ shifts by as much as 0.5 eV with film thickness in the range of $2 < \hbar\omega < 2.5$ eV (Fig. 2 (a)).

To further understand the origin of the thickness-dependence of $\tilde{\epsilon}(\omega)$ we analyzed CMO films of comparable thicknesses, but deposited on LAO and SLAO. The in-plane lattice parameter of SLAO is closest to CMO and the films deposited on SLAO are under less strain compared to STO (Table I). The peak value of the real and imaginary parts of $\tilde{\epsilon}(\omega)$ are larger for a film deposited on SLAO than for a film of comparable thickness deposited on STO (Fig. 3). LAO has an in-plane lattice constant intermediate to SLAO and STO and films deposited on LAO are less strained than those deposited on STO but are under more strain than those on SLAO. This results in a peak value of $\tilde{\epsilon}(\omega)$ intermediate to that of films of similar thickness deposited on SLAO and STO (Fig. 3). In Fig. 3(c) the imaginary part of $\tilde{\epsilon}(\omega)$ for each film in this study is normalized to the bulk value at a photon energy of 2 eV and plotted vs. film thickness. The results indicate that the rate of the increase of the imaginary part of $\tilde{\epsilon}(\omega)$ (ϵ_2) varies differently with persistence of strain coherency and

relaxation, approaching bulk CMO for the thickest films. GIXRD data (Table I) indicate that both SLAO films and both LAO films are fully strained to the substrate, yet we still observe an evolution of $\tilde{\epsilon}(\omega)$, particularly the imaginary portion (Fig. 3(b)). If strain was the dominant effect, we would expect ϵ_2 to be the same for a given strain state.

Particularly in the films of around 5 nm thickness, equilibrium surface atomic structure and electronic wavefunction mixing of the substrate with the bottom several unit cells of CMO can contribute in addition to strain. DFT calculations were performed, considering several candidate structures. To provide further insight into the primary origin of the thickness-dependence we calculated $\tilde{\epsilon}(\omega)$ in the in-plane direction for four and six unit-cell supercells of CMO. We first omitted contributions from strain from a substrate to determine the effect of energy-minimized surface truncation on $\tilde{\epsilon}(\omega)$. Remarkably, the effect is very pronounced for a four unit-cell (around 3.2 nm-thick) film, and considerably weaker for the 6 unit-cell (around 4.8 nm-thick) film (Fig. 4(a)). Incorporation of epitaxial strain (Fig. 4(b)) by introducing STO into a four unit-cell supercell, $(\text{CMO})_4(\text{STO})_4(\text{CMO})_4$, with no free surface, reduces $\epsilon_i(\omega)$, but less than the reduction with a $(\text{CMO})_4$ supercell with one free surface. Significantly, for the 4 unit cell CMO film with a free, vacuum-terminated surface, the effect of including substrate strain, $(\text{CMO})_4(\text{STO})_4(\text{CMO})_{4\text{surface}}$, is negligibly small (Fig. 4(b)). This analysis was repeated for thin films strained by a LAO substrate (Fig. 4(c)), producing the same results.

First-principles calculations were performed by using DFT as implemented in the Vienna Ab Initio Simulation Package (VASP)[24, 25]. The electron exchange and correlation were approximated by the generalized gradient approximation revised for solid (PBEsol)[26] and we adopted an effective on-site Coulomb repulsion $U - J = 3.0$ eV for the d orbitals of Mn atoms [27]. The Kohn-Sham equations were expanded by plane-wave bases truncated at a cutoff energy of 500 eV. A k -point mesh of $6 \times 6 \times 1$ was used in both the calculation of the $(\text{CMO})_4(\text{STO})_4(\text{CMO})_4$ supercell and the calculation of the surface between this supercell and vacuum ($(\text{CMO})_4(\text{STO})_4(\text{CMO})_{4\text{surface}}$), in which vacuum is approximated by 10 Å distance along the [001] direction within the periodic boundary condition. For the studies of bulk CMO, a denser k -point mesh of $6 \times 6 \times 4$ was used. The lattice constant c along the [001] direction as well as all the atomic positions are fully relaxed with the remaining Hellman-Feynman force being less than 1 meV/Å.

According to the first-principles calculations, the difference in dielectric function between

a large and a small CMO supercell originates from a structural reconstruction on the surface between the supercell and the vacuum, the energy associated with the reconstruction being ~ 3 eV. This value is much larger than 0.07 eV, which is the computed energy difference between bulk G-type antiferromagnetic CMO at zero temperature and paramagnetic bulk CMO at room temperature. These are modeled by the structural parameters relaxed to the ground state and using an approximate paramagnetic spin configuration [28], with structural parameters taken from the experiment performed at room temperature by Bozin et al [29]. Thus, our experimental results can be qualitatively interpreted by the first-principles calculations at 0 K assuming the G-type antiferromagnetic configuration.

The thickness dependence of $\tilde{\epsilon}(\omega)$ correlates well with strain relaxation and surface contribution. However, other possible contributions must be considered. For example, CMO exhibits magnetic ordering, but the Néel temperature in bulk CMO, $T_{N, \text{CMO}}$, is around 130 K ($\ll 300$ K) [30], and it is highly unlikely that strain and/or finiteness of the film allows magnetic ordering at 300 K. It has been demonstrated that under high tensile strain oxygen vacancy formation in CMO is favored [31], which could alter band energies. These changes in band energies could alter the electronic and optical properties of thin films and their contribution, although not addressed in this work, cannot be ruled out.

We have shown through spectroscopic ellipsometry measurements that $\tilde{\epsilon}(\omega)$ decreases in value as the CMO films decrease in thickness which would tend to increase the strain state. We observed that for the thinnest films this evolution of $\tilde{\epsilon}(\omega)$ continues even under the same strain state. Taken together, our DFT results, combined with the spectroscopic ellipsometry analysis of the films, indicate that, in the thinnest films, the surface contribution is dominant, whereas in the thicker films, progressive partial and full strain relaxation dominates the evolution of $\tilde{\epsilon}(\omega)$. The interplay among thickness-driven large surface and substrate-induced strain contributions to $\tilde{\epsilon}(\omega)$ in an epitaxial perovskite oxide thin film in its non-magnetic phase holds promise for a novel route to thickness-induced engineering of optical properties.

A. Acknowledgments

The authors acknowledge the Air Force Office of Scientific Research under FA9550-13-1-0124. J.E.S. also acknowledges the U.S. Army Research Office for support of A.R.A. under W911NF-14-1-0500. J.E.S. thanks C. L. Schauer for permitting access to the spectroscopic

ellipsometer.

-
- [1] E. Bousquet, N. A. Spaldin, and P. Ghosez, *Phys. Rev. Lett.* **104**, 037601 (2010).
- [2] S. Bhattacharjee, E. Bousquet, and P. Ghosez, *Physical review letters* **102**, 117602 (2009).
- [3] J. Haeni, P. Irvin, W. Chang, R. Uecker, P. Reiche, Y. Li, S. Choudhury, W. Tian, M. Hawley, B. Craigo, et al., *Nature* **430**, 758 (2004).
- [4] K. J. Choi, M. Biegalski, Y. L. Li, A. Sharan, J. Schubert, R. Uecker, P. Reiche, Y. B. Chen, X. Q. Pan, V. Gopalan, et al., *Science* **306**, 1005 (2004).
- [5] Y. Lu, J. Klein, F. Herbstritt, J. B. Philipp, A. Marx, and R. Gross, *Phys. Rev. B* **73**, 184406 (2006).
- [6] D. Gutiérrez, G. Radaelli, F. Sánchez, R. Bertacco, and J. Fontcuberta, *Phys. Rev. B* **89**, 075107 (2014).
- [7] L. Marín, L. A. Rodríguez, C. Magén, E. Snoeck, R. Arras, I. Lucas, L. Morellón, P. A. Algarabel, J. M. De Teresa, and M. R. Ibarra, *Nano Letters* **15**, 492 (2015).
- [8] D. J. Singh, Q. Xu, and K. P. Ong, *Applied Physics Letters* **104**, 011910 (2014).
- [9] M. D. Scafetta, A. M. Cordi, J. M. Rondinelli, and S. J. May, *Journal of Physics: Condensed Matter* **26**, 505502 (2014).
- [10] H. Liu, M. Lin, Y. Cai, C. Tung, and Y. Chu, *Applied Physics Letters* **103**, 181907 (2013).
- [11] J. Jung, K. Kim, D. Eom, T. Noh, E. Choi, J. Yu, Y. Kwon, and Y. Chung, *Physical Review B* **55**, 15489 (1997).
- [12] N. Loshkareva, L. Nomerovannaya, E. Mostovshchikova, A. Makhnev, Y. P. Sukhorukov, N. Solin, T. Arbuzova, S. Naumov, N. Kostromitina, A. Balbashov, et al., *Physical Review B* **70**, 224406 (2004).
- [13] M. Molinari, D. A. Tompsett, S. C. Parker, F. Azough, and R. Freer, *Journal of Materials Chemistry A* **2**, 14109 (2014).
- [14] T. Günter, E. Bousquet, A. David, P. Boullay, P. Ghosez, W. Prellier, and M. Fiebig, *Phys. Rev. B* **85**, 214120 (2012).
- [15] J. Du, T. Zhang, F. Cheng, W. Chu, Z. Wu, and J. Chen, *Inorganic Chemistry* **53**, 9106 (2014).
- [16] X. Han, Y. Hu, J. Yang, F. Cheng, and J. Chen, *Chemical Communications* **50**, 1497 (2014).
- [17] A. Dejneka, M. Tyunina, J. Narkilahti, J. Levoska, D. Chvostova, L. Jastrabik, and V. Trepakov,

- Physics of the Solid State **52**, 2082 (2010).
- [18] A. Roy, S. Mukherjee, S. Sarkar, S. Auluck, R. Prasad, R. Gupta, and A. Garg, Journal of Physics: Condensed Matter **24**, 435501 (2012).
- [19] E. Chernova, O. Pacherova, D. Chvostova, A. Dejneka, T. Kocourek, M. Jelinek, and M. Tyunina, Applied Physics Letters **106**, 192903 (2015).
- [20] D. Saldana-Greco, C.-W. Lee, D. Yuan, and A. M. Rappe, arXiv preprint arXiv:1504.05251 (2015).
- [21] H. G. Tompkins and W. A. McGahan, *Spectroscopic Ellipsometry and Reflectometry* ((Wiley, New York, 1999).
- [22] C. M. Nelson, M. Spies, L. S. Abdallah, S. Zollner, Y. Xu, and H. Luo, Journal of Vacuum Science & Technology A **30**, 061404 (2012).
- [23] L. Nomerovannaya, A. Makhnev, and A. Balbashov, Physics of the Solid State **48**, 308 (2006).
- [24] G. Kresse and J. Furhmüller, Phys. Rev. B **47**, R558 (1993).
- [25] G. Kresse and J. Furthmüller, Physical Review B **54**, 11169 (1996).
- [26] J. P. Perdew, A. Ruzsinszky, G. I. Csonka, O. A. Vydrov, G. E. Scuseria, L. A. Constantin, X. Zhou, and K. Burke, Physical Review Letters **100**, 136406 (2008).
- [27] J. Hong, A. Stroppa, J. Íñiguez, S. Picozzi, and D. Vanderbilt, Phys. Rev. B **85**, 054417 (2012).
- [28] X. Lu, X. Wu, and H. Xiang, Physical Review B **91**, 100405 (2015).
- [29] E. Božin, A. Sartbaeva, H. Zheng, S. Wells, J. Mitchell, T. Proffen, M. Thorpe, and S. Billinge, Journal of Physics and Chemistry of Solids **69**, 2146 (2008).
- [30] M. Nicastro and C. Patterson, Physical Review B **65**, 205111 (2002).
- [31] U. Aschauer, R. Pfenninger, S. M. Selbach, T. Grande, and N. A. Spaldin, Physical Review B **88**, 054111 (2013).
-

TABLE I: Structural parameters of CMO films. Thickness (t) was determined from XRR and VASE. Film in-plane lattice parameter (a) is extracted from GIXRD (for films thinner than 30 u.c.) or RSM (for films thicker than 100 u.c.) characterization and data fitting. Surface roughness was determined from XRR.

Substrate	t, XRR (nm)	t, VASE (nm)	a (\AA)	Tensile Strain%	Unit Cells	Film Surface Roughness (nm)
STO	4.1	4.1	3.91	5.1	11	0.18
	5.8	5.8	3.91	5.1	16	0.142
	7.1	7.1	3.9	4.8	19	0.185
	10.4	10.4	3.76	1.1	28	0.188
	62.9	62.8	3.75	0.8	169	0.165
LAO	9.6	9.5	3.79 ^a	1.9	26	0.854
	4.9	4.3	3.79 ^a	1.9	13	0.236
SLAO	9.0	10.0	3.75 ^a	0.8	24	0.085
	4.3	4.2	3.75 ^a	0.8	11	0.366

^aGIXRD data indicate that films grown on SLAO and LAO are fully strained to the substrate for both the thick and thin film. The lattice parameter given is that for the substrate.

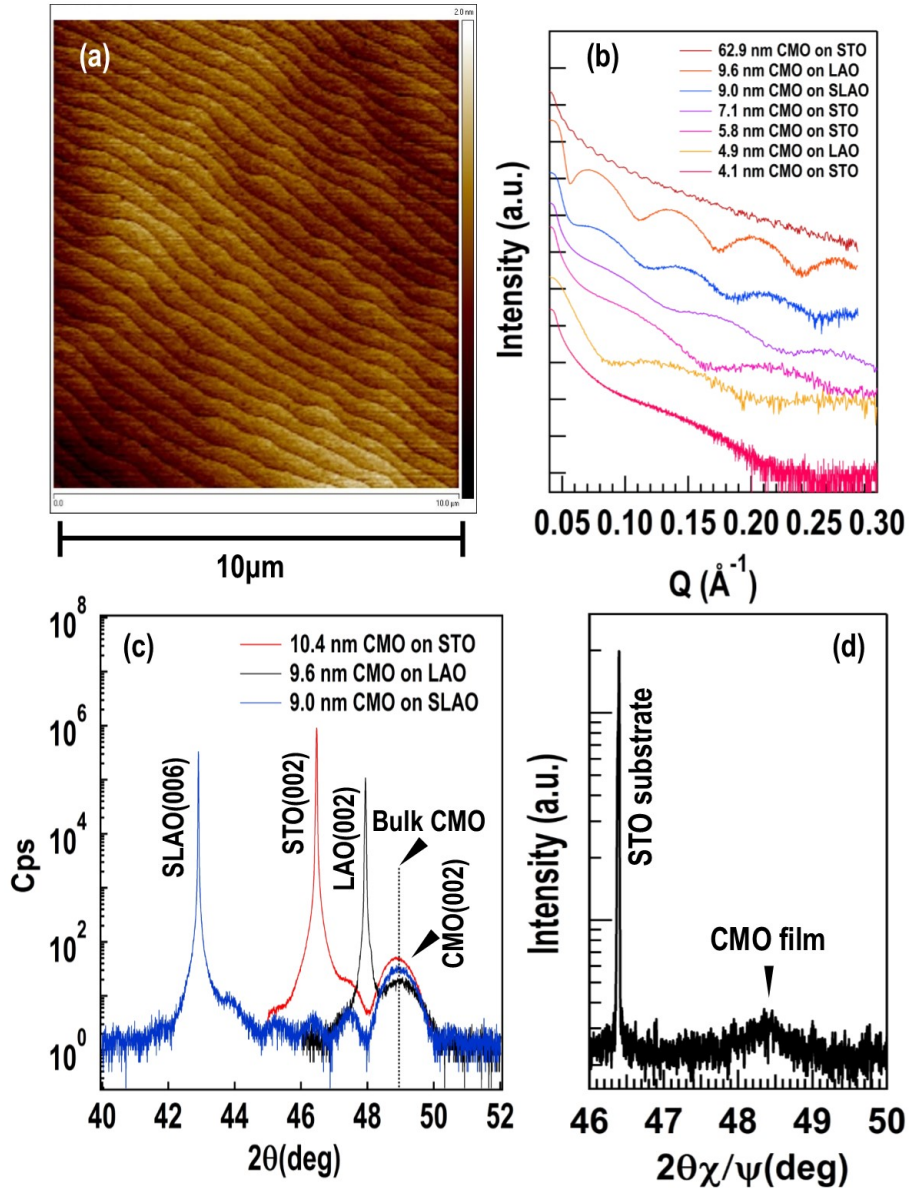


FIG. 1: (a) AFM, (b) XRR, (c) XRD and (d) GIXRD data of CMO films with varying thickness grown on different substrates. (a) AFM of 10.4 nm thick CMO film on STO showing the underlying terraces from the annealed STO substrate. (b) The XRR spectra for films with different thickness on STO, LAO and SLAO substrates. (c) The $2\theta/\omega$ scan of CMO thin films (around 10 nm in thickness) on each substrate. Substrate peaks, bulk CMO peak (dashed line), and film peaks are identified. The CMO film peak on STO is the closest to the bulk value compared to that on the LAO and SLAO substrates. (d) GIXRD spectra of a 10.4 nm thick CMO film grown on STO substrate. Substrate peak and film peak are marked.

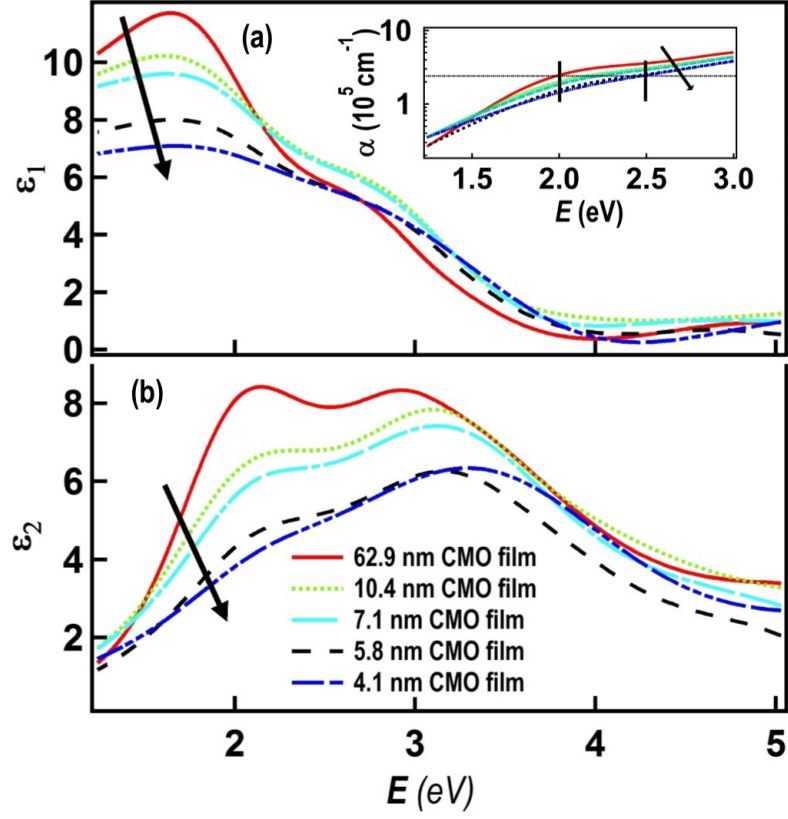


FIG. 2: (a) real, ϵ_1 , and (b) imaginary part, ϵ_2 , of the experimentally determined complex frequency-dependent dielectric function as a function of photon energy for different film thicknesses, on STO(001). The arrow denotes films of decreasing thickness, as specified in Table I. The real and imaginary parts decrease for decreasing film thickness, particularly in the lower energy regime. The thinnest two films are strain coherent, as the films increase in thickness they begin to strain relax. The inset shows α plotted on a semi-log scale over the range 1.2 - 3 eV. At a fixed value of absorption (dashed line shows $\alpha = 2.5 \times 10^5 \text{ cm}^{-1}$) there is as much as a ~ 0.5 eV spectral shift in the photon energy for decreasing film thickness.

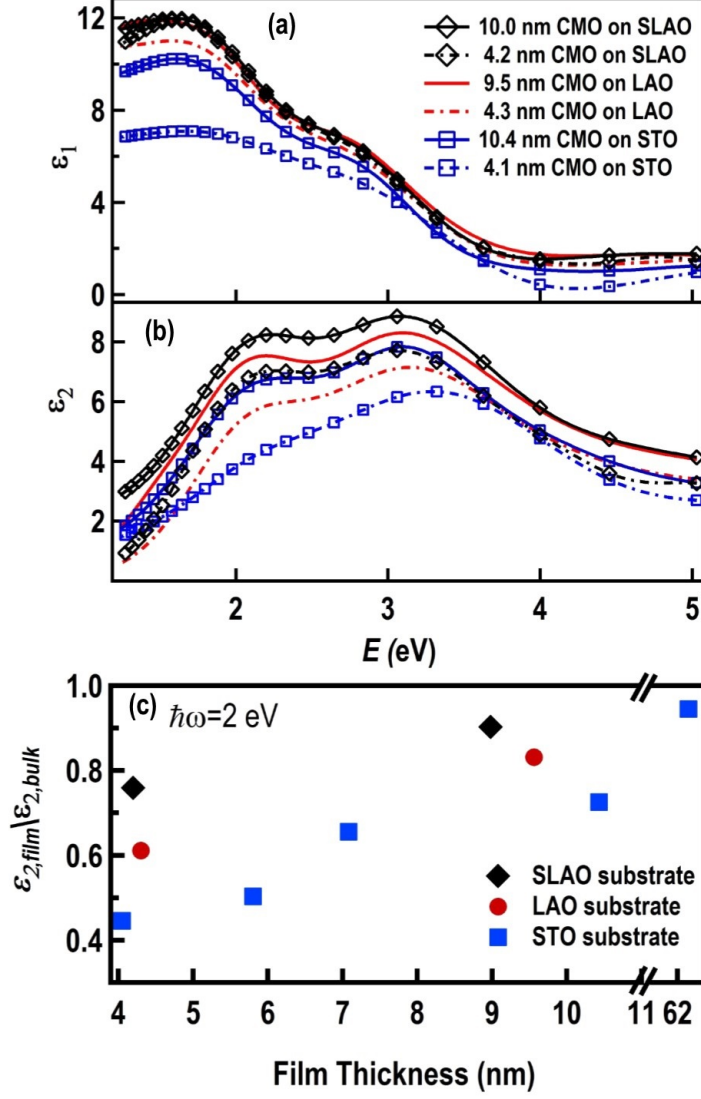


FIG. 3: (a) real, ϵ_1 , and (b) imaginary part, ϵ_2 , of the experimentally determined complex frequency-dependent dielectric function as a function of photon energy for different film thicknesses on three different substrates. The SLAO substrate has an in-plane lattice parameter ($a = 3.75 \text{ \AA}$) closest to bulk CMO ($a = 3.72 \text{ \AA}$), STO ($a = 3.905 \text{ \AA}$) has the largest difference in lattice parameter and LAO ($a = 3.79 \text{ \AA}$) is intermediate between STO and SLAO. The dielectric function of the CMO/SLAO (diamond marker) is closest of that of bulk CMO as compared to CMO grown on LAO (no marker) or STO (square marker). Thicker films are shown with a solid line, the thinner films are shown with a dashed line. (c) a scatter plot of the evolution in (ϵ_2) at 2 eV, normalized to the bulk value, with film thickness for all of the samples.

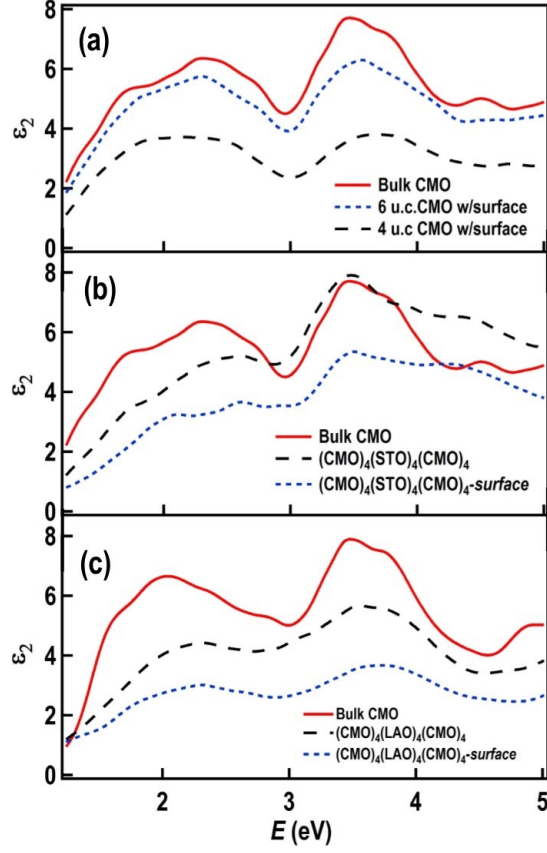


FIG. 4: (a) The effect of free energy-minimized surface termination on the imaginary part of the complex dielectric function (ϵ_2) in the in-plane lattice direction for four- and six-unit cell structures with a free surface as compared to that for bulk CMO. (b) ϵ_2 in the in-plane lattice direction incorporating epitaxial strain by introducing STO into the supercell both with no free surface ($(\text{CMO})_4(\text{STO})_4(\text{CMO})_4$) and one free surface ($(\text{CMO})_4(\text{STO})_4(\text{CMO})_4\text{-surface}$). (c) ϵ_2 in the in-plane lattice direction incorporating epitaxial strain by introducing LAO into the supercell both with no free surface ($(\text{CMO})_4(\text{LAO})_4(\text{CMO})_4$) and one free surface ($(\text{CMO})_4(\text{LAO})_4(\text{CMO})_4\text{-surface}$).